Dark hole and planet detection: laboratory results using the Self-Coherent Camera

Pierre Baudoz[a] and Johan Mazoyer[a] and Marion Mas[a] and Raphaël Galicher[b, c] and Gérard Rousset[a]

[a]Laboratoire d'Etudes Spatiales et d'Instrumentation en Astrophysique, Observatoire de Paris-Meudon, 5 Place Jules Janssen, 92195 Meudon, France;
[b]National Research Council Canada, Herzberg Institute of Astrophysics, 5071 West Saanich Road, Victoria, BC, V9E 2E7, Canada;
[c]Dept. de Physique, Université de Montréal, C.P. 6128 Succ. Centre-ville, Montréal, Qc, H3C 3J7, Canada;

ABSTRACT

Direct imaging and low-resolution spectroscopy of extrasolar planets are exciting but challenging scientific applications of coronagraphy. While the angular separation is well within the reach of actual telescope in the near IR or visible, the planet-star contrast (from 10^{-6} to 10^{-10}) requires wavefront quality and stability hard to reach even with a well-polished space telescope. Several solutions have been proposed to tackle the speckle noise introduced by the residual optical defects. While some concepts rely only on active wavefront correction using deformable mirror, other techniques are based on post-processing and subtract a reference image recorded sometimes simultaneously with the science image. One interesting solution is to choose a concept that allows both active correction and post-processing of high contrast coronagraphic images. This is the case of the Self Coherent Camera (SCC), which has been proposed for the project of space coronagraph SPICES and for the ground-based planet finder EPICS studied for the European Extremely Large Telescope. After recalling the SCC principle, we present both monochromatic and modest bandwidth (2%) experimental results of Dark Hole in the focal plane using a SCC. Example of a post-processing result with SCC is also given to emphasize the interest of combining it with active correction.

Keywords: Exoplanet, Coronagraph, High contrast imaging

1. INTRODUCTION

Understanding the formation and evolution of exoplanetary systems is one of the few major challenges of current astrophysics. The international community has started to simultaneously improve theoretical works and develop dedicated facilities from the ground and from space. High contrast direct imaging has an important role to play in the completion of indirect detection techniques such as transits and radial velocities. Today, a few young planets at large separations have already been detected[1, 2] and their characterization is starting. Ultimately, direct detection could allow us to fully characterize the properties of exoplanets, including indications of habitability, and physics and chemistry of their atmosphere. The required contrast capability for exoplanet imaging is the main limitation to discoveries in this field. The first generation of ground-based instruments dedicated to high contrast imaging is currently being developed both in Europe and in North America by large international consortia.[3, 4] These instruments are now close to starting operations, with an expected contrast performance better than 10^{-6} to 10^{-7} for detecting young Jupiter-like planets within 0.5 arcsec from their star, well inside the stellar halo.

A large improvement of the performance is mandatory to study lower mass planets like Neptunes or possibly rocky planets. This is one of the key motivation for the future extremely large telescopes (ELT), the dominant infrastructures of tomorrow's optical and infrared astronomy from the ground. Space-based projects based on coronographic telescopes have also been proposed to directly image such faint planets. The stable environment

Send correspondence to P. Baudoz: E-mail: Pierre.Baudoz@obspm.fr

and the absence of atmospheric turbulence makes these projects the most promising instruments to detect earth-twins.

The contrasts of the latter planets require a deep understanding of the limitations for high contrast imaging and new technological solutions that can self-calibrate the observations. One solution proposed for the direct planet detection on ELT[5] or on space-based projects[6] is the Self-Coherent Camera (SCC). The SCC is a concept of high contrast imaging instrument[7] that takes benefit from the coherence between the stellar leakage speckles and the stellar light rejected by a coronagraph. This property of coherence is used to measure the electric field in the final focal plane [8] or detect a planet among the speckles by post-processing.[7]

We have recently developed a laboratory bench to estimate the performance of the SCC on a real setup. In this paper, after recalling the principle of the SCC, we present how we estimate the focal plane electric field directly from the SCC focal plane image and how we minimize it using a deformable mirror located in a pupil plane upstream of the coronagraph. Then, we describe a simple method to improve the contrast of the image by post-processing using the SCC fringes. After a brief description of the test bench, we present laboratory results for both minimization and post-processing methods and compare the first one to numerical simulations.

2. DARK HOLE CORRECTION WITH THE SELF-COHERENT CAMERA

2.1 Principle and simplified formalism for the Self-Coherent Camera
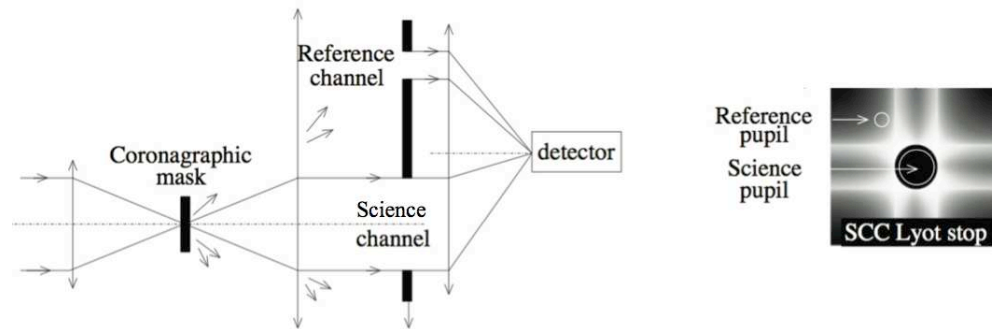

Figure 1. Principle of the SCC coupled with a Four Quadrant Phase Mask (FQPM) coronagraph.[9] The image on the right shows the light distribution in the pupil plane downstream the coronagraphic focal plane.

A robust design can associate the SCC with most of the coronagraphs by simply modifying the Lyot stop geometry.[8] The principle of the SCC coupled with a Four Quadrant Phase Mask (FQPM) coronagraph[9] is shown in Figure 1. The SCC simply modify the Lyot stop by adding a reference pupil (Figure 1). As in the classical Lyot coronagraph, the star is focalized on a coronagraphic mask. In the pupil downstream of the focal plane mask, an unaberrated stellar light is fully diffracted outside of the pupil geometry.[10] When the beam upstream the coronagraph is aberrated, there is also residual light in the science pupil (classical Lyot stop) that can interfere with light from the reference pupil to create fringed speckles on the detector. Theses fringes can be used to measure the focal plane electric field but also to discriminate speckles from a planet that is not fringed.

Below, we describe briefly the formalism that describes the intensity in the focal plane for a SCC. Following the formalism given in Galicher et al. 2008 and 2010,[6,8] we can write the monochromatic interferential image on the detector I:

$$I(\alpha) = |A_S(\alpha)|^2 + |A_R(\alpha)|^2 + A_S(\alpha)A_R(\alpha)^* \exp\left(\frac{2i\pi\alpha\xi_0}{\lambda_0}\right) + A_S(\alpha)^*A_R(\alpha)\exp\left(\frac{-2i\pi\alpha\xi_0}{\lambda_0}\right) \qquad (1)$$

where $A_S(\alpha)$ and $A_R(\alpha)$ are the complex amplitudes in the focal plane that propagate through the science pupil and the reference pupil respectively. α is the focal plane angular coordinate, λ_0 is the wavelength considered and ξ_0 is the distance between the two pupils.

Let's rewrite I:

$$I(\alpha) = I_S(\alpha) + I_R(\alpha) + I_-(\alpha)\exp\left(\frac{2i\pi\alpha\xi_0}{\lambda_0}\right) + I_+(\alpha)\exp\left(\frac{-2i\pi\alpha\xi_0}{\lambda_0}\right) \tag{2}$$

The intensity I_S is the intensity of the stellar residual we would get if no reference pupil was added to the Lyot stop in the pupil plane downstream the coronagraph. I_R is the intensity that can be measured if the Lyot stop is occulted. I_- and I_+ are complex functions that are describing the modulated part of the SCC image. $I_-(\alpha)$ is a linear function of the complex amplitudes $A_S(\alpha)$ which directly measures the electric field in the focal plane that we would get with a simple coronagraph:

$$I_-(\alpha) = A_S(\alpha)A_R(\alpha)^* \tag{3}$$

The Fourier transform of an SCC image ($F[I]$, F describing the direct Fourier transform) shows 3 distinct parts if $\xi_0 > 3D_L/2 + D_R/2$ with D_L the Lyot diameter and D_R the reference pupil diameter.[6,8] These 3 parts corresponds to the Fourier transform of $I_S + I_R$ for the central peak and the Fourier transform of I_- and I_+ for the lateral peaks (an example of $F[I]$ is given in Fig. 3, left).

2.2 Step followed to estimate $I_-(\alpha)$

In this section, we describe how to extract the modulated part $I_-(\alpha)$ (or $I_+(\alpha)$) from $I(\alpha)$.

1. Calculate the Fourier transform of $I(\alpha)$: $F[I(\alpha)]$

2. Multiply $F[I(\alpha)]$ by a numerical mask that put to zero every pixels but the one corresponding to $F[I_-(\alpha)]$ in both the real and imaginary part (red circles in Fig. 3, left). Note that the diameter of the zone extracted is defined experimentally but is given by the size of the intercorrelation of the Lyot stop and the reference pupil (theoretical diameter equal to $D_R + D_L$).

3. Shift this image to recentre this modulated part

4. Resize the image by dropping zero rows and columns to set the sampling of the Fourier transform of this modulated part to 2 pixels per λ/D. This helps minimizing the size of the vector that measures $I_-(\alpha)$.

5. Calculate inverse Fourier transform of this new image.

6. Extract only the electric field that can be corrected by the DM (Fig. 3, right). For a NxN, DM, this corresponds to a field of NxN λ/D, i.e. $8N^2$ pixels for both real and imaginary part if the sampling has been optimized to 2 pixels per λ/D like it is described in step 4.

2.3 Formalism for the Dark Hole minimization

We propose to improve the performance of the coronagraph by minimizing the complex amplitude $A_S(\alpha)$ in a selected area called Dark Hole (DH)[11,12] by applying phase correction on a deformable mirror (DM) located upstream of the coronagraph. Since the correction by the Deformable mirror (DM) is limited to a field of $N\lambda/D_L$x$N\lambda/D_L$ for a DM with NxN actuators, the DH maximum size is $N\lambda/D_L$x$N\lambda/D_L$.

2.3.1 Hypotheses

The light diffracted outside of the pupil geometry downstream of the focal plane coronagraph only depends on the coronagraphic mask placed in the focal plane. Thus, the amplitude and phase of the reference electric field that is diffracted by the reference pupil is stable inside the DH as far as the amplitude and phase defects are small.[6] Thus, even if the illumination of A_R is not constant over the DH, it can be considered as a function that has no time variation during correction. Thus, minimizing $A_S(\alpha)$ over the DH is equivalent to minimize $I_-(\alpha)$ applying a ponderation function(here $A_R(\alpha)$) on $A_S(\alpha)$.

Since the complex amplitude $A_R(\alpha)$ is diffracted from a pupil with a relatively small diameter ($D_R < D_L$), its focal plane extension is rather large. If we choose D_R small enough to get only the central part of the reference

diffraction pattern inside the square field of Nλ/D_LxNλ/D_L, this ensure that $A_R(\alpha)$ never reaches zero inside the DH. It sets a requirement on D_R:

$$D_R < 1.22\frac{\sqrt{2}D_L}{N} \tag{4}$$

Remembering that $A_S(\alpha)$ is a linear function C of the complex amplitude in the pupil plane upstream of the coronagraph where is located the DM, we can write (C is essentially made of Fourier transforms and multiplication by a Lyot stop and a phase mask) :

$$A_S(\alpha) = C(P\exp(a + i(\phi + \phi_{DM})) \tag{5}$$

P is the usual top-hat distribution describing the pupil. ϕ and a describe the phase and amplitude in the pupil plane upstream of the coronagraph and ϕ_{DM} is the phase introduced by the DM. Assuming small phases (ϕ and ϕ_{DM}) and small amplitude (a), we can simplify Eq. 5:

$$A_S(\alpha) = C(P\exp a + i(\phi + \phi_{DM})) \approx C(P) + C(a) + iC(\phi) + iC(\phi_{DM}) \tag{6}$$

Thus A_S and by extension $I_-(\alpha)$ are linear functions of the phase ϕ_{DM} introduced in the DM.

2.3.2 Interaction matrix and control matrix

To link the measured complex amplitude in the focal plane $I_-(\alpha)$ with the applied correction on the DM, we choose to build an interaction matrix that record $I_-(\alpha)$ for series of applied ϕ_{DM} (or voltages). We choose to use the Fourier basis to build this interaction matrix. Thus, we apply cosinus and sinus function on the DM as described in Poyneer et al. 2005.[13] Each period of a cosinus (or a sinus) applied on the DM corresponds to a given spatial frequency in the focal plane (Fig 2). In intensity, the Point Spread Function that appears at this frequency is identical for the cosinus and the sinus. The electric field when applying a cosinus or a sinus on the DM is however different and this can be measured on $I_-(\alpha)$.
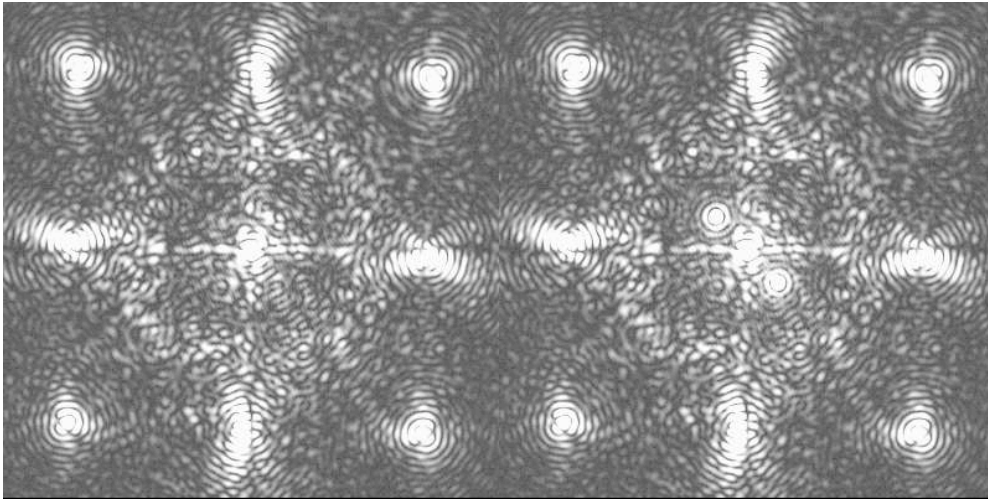

Figure 2. Left: SCC image with partially corrected wavefront ($I^\phi(\alpha)$). Right: SCC image when adding one of the cosinus mode on the DM ($I^{\phi+\cos}(\alpha)$). Both images are laboratory images recorded on the test bench (see Sect.3.1).

The cosinus function adds to the phase of the instrument and a difference between images with cosinus (or sinus) ($I^{\cos}(\alpha)$) and without ($I(\alpha)$) is mandatory to recover the cosinus information among the general phase. To build the interaction matrix, we record for each Fourier mode an image recorded with a flattened DM shape ($I^\phi(\alpha)$, left image in Fig. 2) where the speckles come from phase and amplitude defects from the instrument and one recorded with a cosinus (or sinus) added to the DM shape ($I^{\phi+\cos}(\alpha)$: Fig. 2, right). Applying the steps

described in Sect. 2.2 to extract $I_-(\alpha)$ for both images gives us $I_-^{\phi+\cos}(\alpha)$ and $I_-^{\phi}(\alpha)$. Assuming small phase and amplitude defects, i.e. Eq. 6 is true, the difference between these two extracted $I_-(\alpha)$ is equal to:

$$I_-^{\phi+\cos}(\alpha) - I_-^{\phi}(\alpha) = I_-^{\cos}(\alpha) \tag{7}$$

which corresponds to $I_-(\alpha)$ for a pure cosinus (or sinus) phase. Examples of extracted $I_-(\alpha)$ from recorded images are shown in Fig. 3, right.
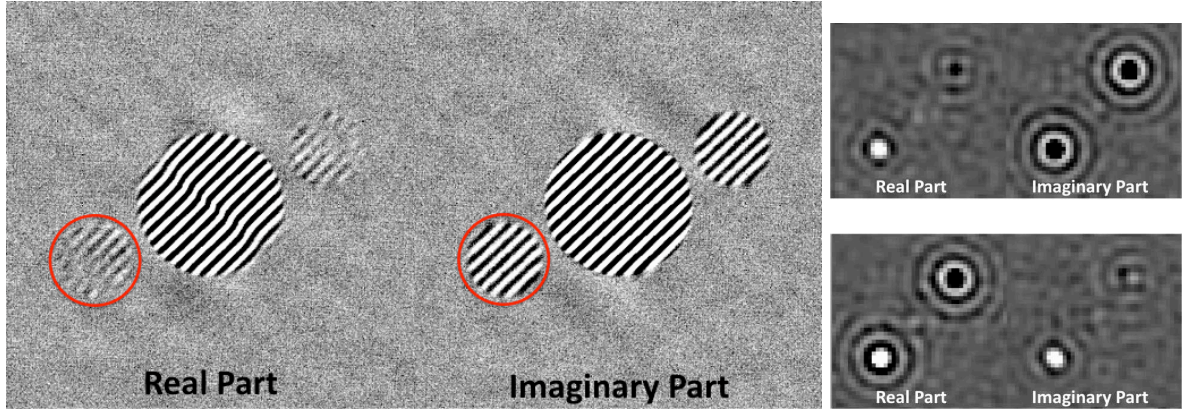

Figure 3. Left: Fourier transform of the difference between an image with a cosinus applied ($I_-^{\phi+\cos}(\alpha)$: Fig. 2, right) and without cosinus applied ($I^{\phi}(\alpha)$: Fig. 2, left). The two lateral peaks correspond to the modulated part of the SCC image. A circle is drawn around the part we extract that correspond to $F[I_-^{\phi+\cos}(\alpha) - I_-^{\phi}(\alpha)]$ Right: Example of the focal plane electric field $I_-(\alpha)$ when a cosinus (on top) or a sinus (on bottom) is applied on the DM. Data of this figure based on laboratory images recorded on the test bench (see Sect.3.1)

We transform the 2D complex image obtained for each frequency into a 1D vector. The final interaction matrix has N^2 row (frequencies in the Fourier basis) and $8N^2$ column (pixels in the focal plane for the DH in $I_-(\alpha)$). When the interaction matrix is built, we inverse it with a least square minimization using Singular Value Decomposition (SVD) to calculate the control matrix. When multiplying this latest matrix by the vector $I_-(\alpha)$ estimated from a recorded image $I(\alpha)$, we directly get the control values to be sent to the DM. We use a simple integrator control low with a relatively low gain ($g < 0.4$) to apply the correction on the DM.

2.4 Formalism for SCC post-processing

However, residual speckles may remain in the focal plane: first outside of the DH and second on one side of the DH if there are amplitude defects.[11] To improve the detection of planets, we can use the fact that the planet is not modulated by fringes while the speckles are, i.e. the planet does not interfere with the light diffracted by the reference pupil. Assuming $I_P(\alpha)$ describes the intensity of the planet, the SCC image in the focal plane can be written starting from Eq. 1:

$$I(\alpha) = I_P(\alpha) + |A_S(\alpha)|^2 + |A_R(\alpha)|^2 + A_S(\alpha)A_R(\alpha)^* \exp\left(\frac{2i\pi\alpha\xi_0}{\lambda_0}\right) + A_S(\alpha)^* A_R(\alpha) \exp\left(\frac{-2i\pi\alpha\xi_0}{\lambda_0}\right) \tag{8}$$

We adopt a strategy of minimization of the difference between the recorded image and a model of our image. Our model image is based on Eq. 1 with estimated $A_S^{est}(\alpha)$, $A_R^{est}(\alpha)$, ξ_0^{est}.

$$I^{est}(\alpha) = |A_S^{est}(\alpha)|^2 + |A_R^{est}(\alpha)|^2 + A_S^{est}(\alpha)A_R^{est}(\alpha)^* \exp\left(\frac{2i\pi\alpha\xi_0^{est}}{\lambda_0}\right) + A_S^{est}(\alpha)^* A_R^{est}(\alpha) \exp\left(\frac{-2i\pi\alpha\xi_0^{est}}{\lambda_0}\right) \tag{9}$$

The term $A_R^{est}(\alpha)$ is based on an image of $I_R(\alpha) = |A_R(\alpha)|^2$ recorded by occulting the lyot stop. Since the image can be noisy, we fit the recorded intensity with a gaussian function $G(\alpha)$. As a result, no detection are practically possible for distance larger than λ/D_R. The phase of $A_R(\alpha)$ inside λ/D_R is certainly not varying much, so we decide to write the estimation of the complex amplitude:

$$A_R^{est}(\alpha) = f_G \sqrt{G(\alpha)} \tag{10}$$

With f_G a coefficient that takes into account possible variation of the reference between the recording of the SCC image and the recording of the reference image.

The term $A_S^{est}(\alpha)$ is estimated directly from $I_-(\alpha)$. We force the phase of $A_S^{est}(\alpha)$ to be the one recorded by $I_-(\alpha)$ but let the amplitude of $A_S^{est}(\alpha)$ free with a error term $\Delta(\alpha)$:

$$A_S^{est}(\alpha) = \left(\frac{I_-(\alpha)}{A_R^{est}(\alpha)} + \Delta(\alpha) \right) \exp\left[i.\arg\left(\frac{I_-(\alpha)}{A_R^{est}(\alpha)} \right) \right] \tag{11}$$

We simply estimate by hand the distance ξ_0^{est} from the Fourier transform of $I(\alpha)$. Our simple minimization criteria can then be written:

$$J(f, \Delta) = \|I(\alpha) - I^{est}(\alpha)\|^2 \tag{12}$$

where $\|x\|^2$ denotes the sum of squared pixel values inside the full DH and where $I^{est}(\alpha)$ is defined by Eq. 9. We minimize J starting with $f_G = 1$ and $\Delta(\alpha) = 0$. Note that the minimization will not be affected by a planet $I_P(\alpha)$ (except by its noise) because it is not modulated. This minimization is rather crude and could be better optimized. However, it already gives encouraging results as shown in Sect. 3.3.

3. TEST BENCH RESULTS

In this section, we are presenting laboratory results recorded on the test bench we developed in Laboratoire d'Etudes Spatiales et d'Instrumentation en Astrophysique (LESIA) at Observatoire de Paris. First, we rapidly recall the main characteristics of the bench.

3.1 Test bench description

The test bench is described in details in Mas et al. 2010.[14] The main components used for the tests presented in this paper are quickly recalled below:

1. An optical fiber source that is fed by a laser diode fiber (@ 635 nm) or a white light source coupled with bandwidth filter. Characteristics of the bandwidth filter used in Sect. 3.3: $\lambda_0 = 638nm$, $\Delta\lambda = 11.3nm$.

2. A fully reflective optical design creating 3 pupil planes where we place:

    (a) An unobscurated entrance pupil plane of 8.1 mm and a tip-tilt mirror

    (b) A Boston Micromachines deformable mirror of 32x32 actuators with a pitch of 0.3 mm. We use only 27x27 actuators to avoid two dead actuators on the DM and have a full pupil free of non-functionning actuators.

    (c) The Lyot stop of 8mm (99% filtering) and a reference pupil of 0.35 mm with $\xi_0 = 13$ mm

3. And 3 focal planes, two of which include:

    (a) A monochromatic Four Quadrant phase mask[9] optimized for 635 nm

    (b) A CCD camera of 640x480 pixels (400x400 used) with a readout noise of 18 e- and a Full Well capacity of 13 000 e-

4. A set of Neutral Density filters to record PSF images (no coronagraph) to normalize the photometry of the coronagraphic images.

5. An additional lens that can be inserted in front of the camera for pupil plane imaging

6. A software (Labview) that can control the DM using control matrix built as described in Sect. 2.3

3.2 Monochromatic Dark Hole correction

First, we present the results for monochromatic light. Applying the correction scheme described in Section 2.3, we can create a DH inside the focal plane of the SCC image (Fig. 4, top center). As expected, we clearly see that the correction is limited to a field of 27x27 λ/D. We estimate the contrast level for each angular distance by calculating the standard deviation in rings of 1 pixel thickness. The normalization is made on the maximum of the non-coronagraphic image which is recorded by moving the source off-axis of the coronagraph. The contrast measured inside the DH reaches 10^{-6} (top curve with diamonds in Fig. 5, left) when trying to correct for the full DH of 27x27 λ/D. These residuals are expected to come from amplitude defects. Thus, if we limit the DH correction to one side of the area that can be corrected by the DM, we should be able to improve largely the contrast.[11]

To apply this one-sided DH correction, we simply use only half of the control matrix that we built for the full DH. To calculate the contrast in this DH, we apply the same calculation than for the full DH (standard deviation in a ring) but restricting the data to the one-sided DH. The resulting contrast in the DH is improved to a contrast of a few 10^{-8} (bottom curve with diamonds in Fig. 5, left). In this one-sided DH, the contrast between 5 and 13 λ/D is estimated to 2.10^{-8} RMS. The image corresponding to this correction is shown in Fig. 4 (top right).

To compare our recorded data with a simulation, we estimate the amplitude defects by recording an image of the pupil illumination (Fig. 5, right). The pupil image is recorded on the final detector by inserting a lens in front of the detector. Thus the illumination measured is only an estimation of the illumination upstream of the coronagraph since it also takes into account amplitude effects downstream of the coronagraph. We can see high frequency structures in the image that have a period corresponding to the DM pitch. The surface of the Boston Michromachines DM is known to have print-through phase effects of a few tens of nanometers peak to valley inside each actuators and etch holes that come from the fabrication process of the DM. However, since the DM is placed in a pupil plane, we are expecting no illumination effects from the phase errors of the mirror. In fact, the structures inside each actuator are diffracting light on a large angle while our bench has a relatively slow beam (F/D=100). As a consequence, part of the light diffracted by these structures are diffracted outside of the optical reflective elements and never reach the final focal plane. These structures are also known to be more pronounced on the edges of the mirror than on the center, which creates a low frequency amplitude error. The level of the amplitude defects is estimated at about 10% RMS in intensity.

We introduce these amplitude defects into a numerical simulation that reproduces the diffraction through a Four Quadrant Phase Mask coronagraph, the minimization of the focal plane electric field, and calculate the simulated radial profiles. Assuming no phase errors (amplitude defects only), the profiles obtained for a full DH and a one-sided DH are shown in Fig. 5 (left, dotted lines). The simulated and recorded data are matching well except close to the center (below $2\lambda/D$) and after the highest correction frequency ($13.5\lambda/D$). At the center, the recorded data are saturated to improve the signal to noise ratio for larger angular distances. The true contrast at 1 λ/D is close to 10^{-4} and there is no real mismatch between simulated and recorded data at the center. For larger angular distances, the mismatch certainly comes from phase errors that are not corrected above $13.5\lambda/D$. Adding a numerical phase error of 20 nm RMS (power spectral density of the phase varying in f^{-3}) to our simulation, we obtain profiles that better reproduce the recorded data. The simulated images using this phase and the measured amplitude defects for both full DH and one-sided DH are shown in Fig. 4 (bottom).

We recognize the same focal plane structures created by the high frequency of the mirror but with a lower level since we only take into account their measured effects on the amplitude while they also have a strong impact on the phase. The radial profiles of these simulated images (solid lines in Fig. 5, left) are matching well the recorded data (diamonds in Fig. 5, left) except close to the center (below $2\lambda/D$) where the recorded data
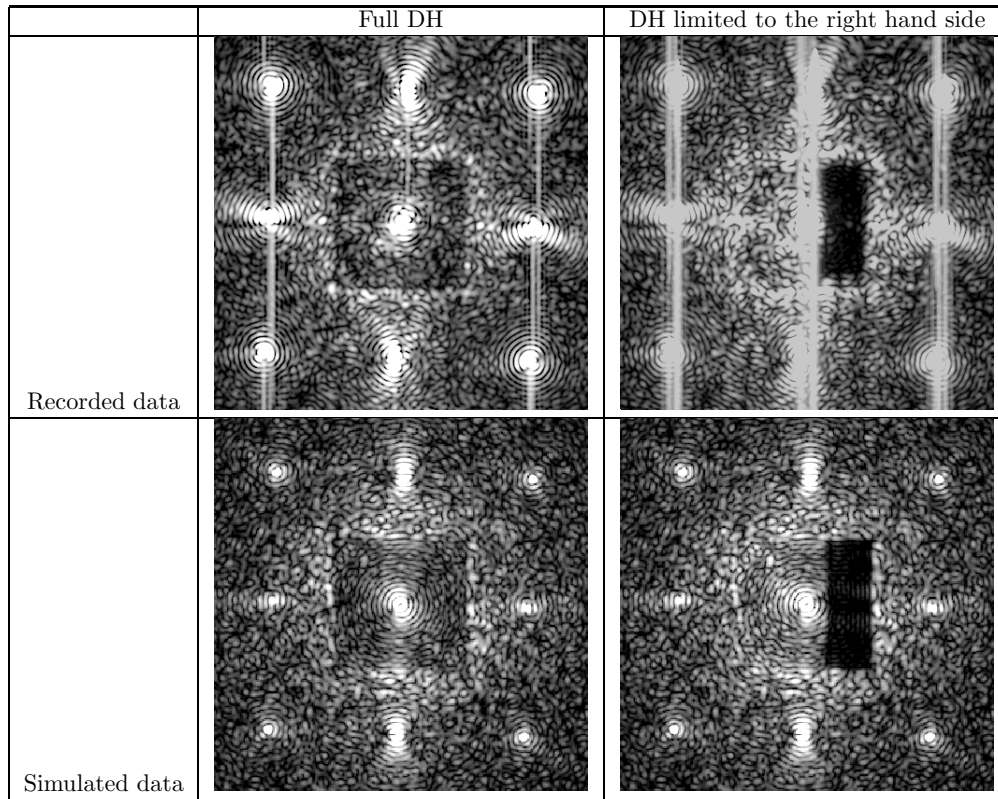
	Full DH	DH limited to the right hand side
Recorded data		
Simulated data		

Figure 4. Comparison between recorded (top) and simulated (bottom) data with correction on the full DH (27x27 λ/D) on the left and limited to a right side DH (-13.5 λ/D to +13.5 λ/D in vertical and 5 λ/D to +13.5 λ/D in horizontal) on the right.
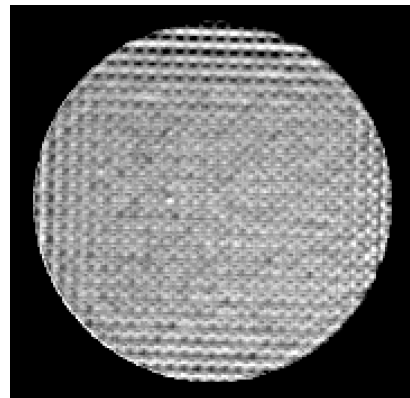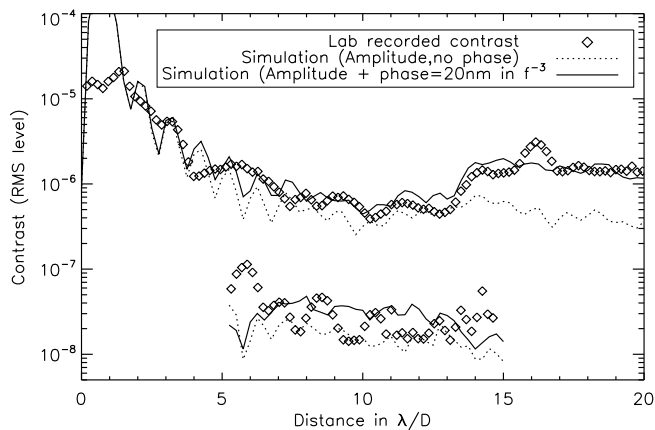

Figure 5. Left: RMS radial profil of focal plane images for the full DH (top curves) and for the one-sided DH (bottom curves) for 3 cases: *Diamonds:* recorded data, *Dotted lines:* simulation with only the recorded amplitude defects introduced, *Solid lines:* simulation with phase and amplitude. Right: Recorded illumination of the pupil without coronagraph.

are saturated. It seems clear that the contrasts reached on the bench are limited by the amplitude defects both for the full DH (10^{-6} RMS) and for the one-sided DH (2.10^{-8} RMS). Thus, with less amplitude defects, we could expect much better results with the Self-Coherent Camera. Most importantly, it shows that the SCC can estimate precisely the electric field since it gives results rather similar to simulation values. It also shows that the SCC measures phase and amplitude defects separately without mixing them.

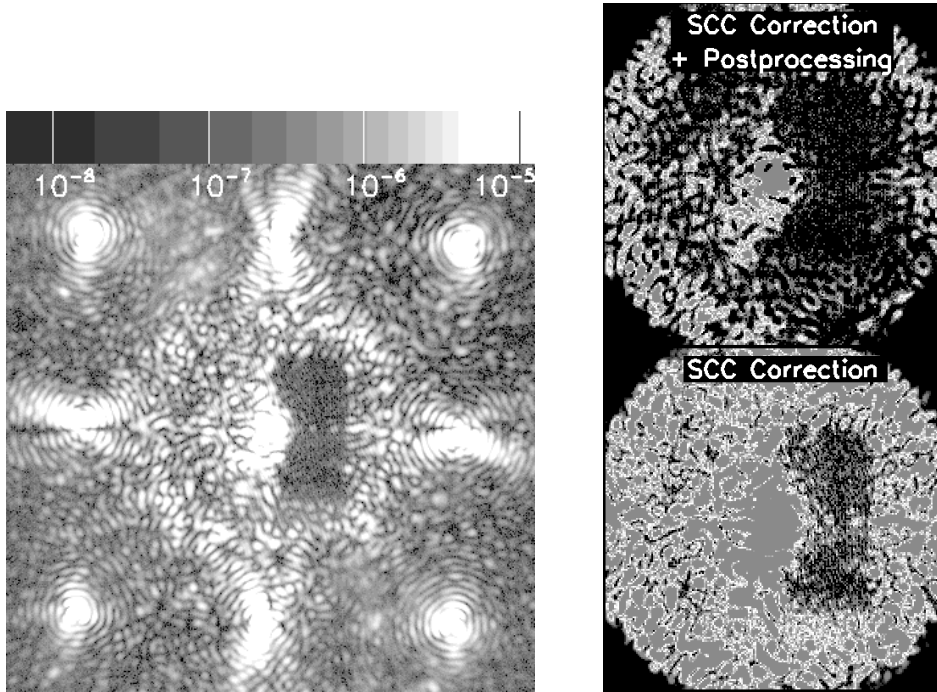## 3.3 Dark Hole correction and Post-processing with narrow spectral bandwidth

Figure 6. Left: Recorded image with a narrow spectral bandwidth (2%) using correction based on electric field minimization. Right bottom: Image with correction only (same image than on the left but with a scale that limit the value to less than 10^{-6}). Right top: Image with correction and post-processing (same scale than the bottom image).

We also tested the SCC correction with a narrow spectral bandwidth (2%). The source is fainter than the laser diode. Thus, the signal to noise ratio on a given recorded image is lower than on monochromatic images and the correction is stopped when the one-sided DH is limited by camera readout noise (Fig. 6, left). The contrast achieved in the DH for this image between $4\lambda/D$ and $13\lambda/D$ is about $1.8 \ 10^{-7}$ (see star curve in Fig. 7) while the average correction over 360° is between 10^{-5} and 10^{-6} (solid line in Fig. 7). Thus, the effects of the amplitude defects strongly decrease the performance of the coronagraph on the left hand side of the image. To improve the detection on this side, the solution is to apply the SCC post processing mode that reap the full benefit of the fringes that encode the residual speckles on both sides in the focal plane. To estimate the intensity of the reference image I_R that is needed for this post-processing mode, we occult the Lyot stop and record series of images to minimize the readout noise. The term $A_R^{est}(\alpha)$ is estimated by fitting a gaussian function on I_R as described in Sect. 2.4. As a result, no improvement of the contrast is expected further than λ/D_R. Thus, we force the outer part of the image (larger than a radius of $20\lambda/D$) to zero. We can clearly see that on the two images in Fig. 6 (right).

Applying the procedure described in Sect. 2.4, we can improve the overall contrast in the image as shown in Fig. 6 (right) where the bottom image corresponds to the DH correction only while top image shows the improvement after post-processing of this corrected image. The contrast is improved by a factor 20 on the left hand side and about 2 on the right hand side. The contrast reaches a value below 10^{-6} all around the star

(dashed line in Fig. 7) and about $8 \ 10^{-8}$ in the DH between 4 and 13 λ/D (diamond curve in Fig. 7). The small improvement on the right hand side is certainly partly limited by the readout noise level that is estimated for this image at $4 \ 10^{-8}$ RMS. Note that the level of noise is estimated after applying the same Fourier filtering on the image than the one automatically applied when calculating $I^{est}(\alpha)$. Indeed, $I^{est}(\alpha)$ is based on the estimation of $A_S^{est}(\alpha)$ (Eq.11) that depends on $I_-(\alpha)$ which is filtered in the Fourier plane by a numerical mask (see steps 2 to measure $I_-(\alpha)$ and described in Sect. 2.2). Even though the left hand side is not perfectly cleaned by the post-processing, the improvement is good enough to enable the detection over the complete DH at a level of a few 10^{-7}. A more symmetrical contrast is very useful not only for improving planet detection strategy but also to image complex structures like faint exozodiacal disks.
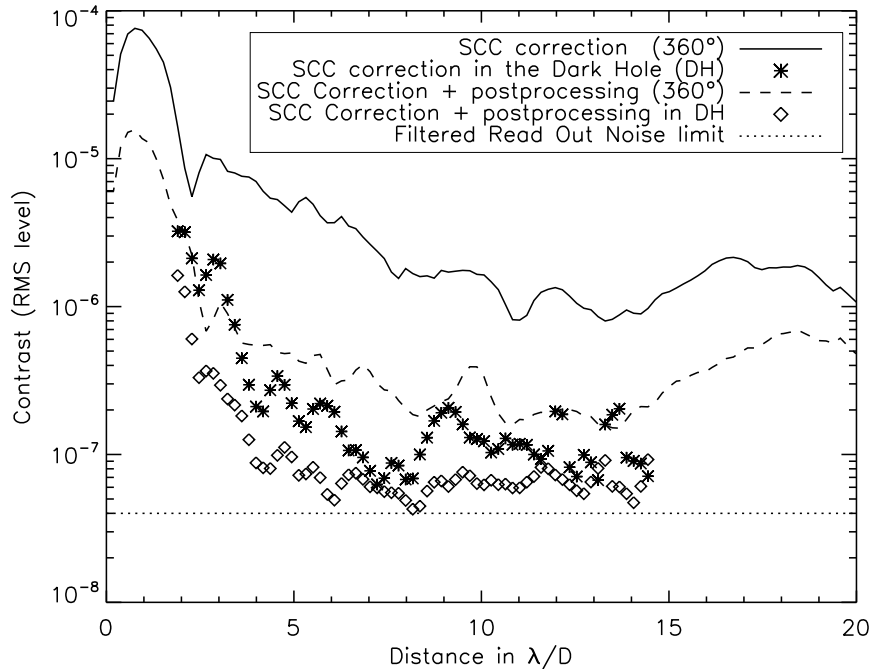

Figure 7. RMS radial profiles estimated for one-sided DH image for raw correction (Fig. 6, right bottom) and for post-processing (Fig. 6, right top). The profiles are calculated over 360° for raw correction (solid line) and post-processing (dashed line). The profiles are also calculated only on the right hand side DH for raw correction (stars) and post-processing (diamonds). The level of the measured readout noise filtered by the post-processing is also drawn (dotted line).

4. CONCLUSION

We demonstrated that the concept of Self-Coherent Camera (SCC) coupled with a Four Quadrant Phase mask coronagraph is working in laboratory environment with monochromatic source, as well as with narrow spectral bandwidth (2%). In monochromatic, minimizing the electric field in the focal plane enables us to reach contrast level of $2 \ 10^{-8}$ between 5 and 13 λ/D on one side of the image. A numerical simulation taking into account the amplitude defects measured on the bench reaches the same limiting level showing that the correction by the DM is optimized in the context of the minimization of the electric field but also that the SCC is an efficient tool to precisely measure the wavefront defects. Contrast in narrow spectral bandwidth reaches a raw level of $1.8 \ 10^{-7}$ between 4 and 12 λ/D possibly limited by the camera readout noise. We showed that the fringes that encode the speckles are a useful tool to improve further the contrast. This SCC post processing applied on the recorded data helped to improve the contrast by a factor 20 on the side of the image limited by the amplitude defects while on the DH side it decreases the contrast from $1.8 \ 10^{-7}$ to $8 \ 10^{-8}$. We may expect better performance

if we decrease the readout noise level (estimated here around $4 \cdot 10^{-8}$ RMS) or if we improve our minimization algorithm that is rather simple for now. More extensive chromatic tests must also be performed to estimate more precisely the overall performance of such an instrument on a telescope.

REFERENCES

[1] Marois, C., Macintosh, B., Barman, T., Zuckerman, B., Song, I., Patience, J., Lafrenière, D., and Doyon, R., "Direct Imaging of Multiple Planets Orbiting the Star HR 8799," *Science* **322**, 1348– (Nov. 2008).

[2] Lagrange, A., Gratadour, D., Chauvin, G., Fusco, T., Ehrenreich, D., Mouillet, D., Rousset, G., Rouan, D., Allard, F., Gendron, É., Charton, J., Mugnier, L., Rabou, P., Montri, J., and Lacombe, F., "A probable giant planet imaged in the β Pictoris disk. VLT/NaCo deep L'-band imaging," *Astronomy & Astrophysics* **493**, L21–L25 (Jan. 2009).

[3] Beuzit, J.-L., Feldt, M., Dohlen, K., Mouillet, D., Puget, P., Wildi, F., Abe, L., Antichi, J., Baruffolo, A., Baudoz, P., Boccaletti, A., Carbillet, M., Charton, J., Claudi, R., Downing, M., Fabron, C., Feautrier, P., Fedrigo, E., Fusco, T., Gach, J.-L., Gratton, R., Henning, T., Hubin, N., Joos, F., Kasper, M., Langlois, M., Lenzen, R., Moutou, C., Pavlov, A., Petit, C., Pragt, J., Rabou, P., Rigal, F., Roelfsema, R., Rousset, G., Saisse, M., Schmid, H.-M., Stadler, E., Thalmann, C., Turatto, M., Udry, S., Vakili, F., and Waters, R., "SPHERE: a planet finder instrument for the VLT," in [*Society of Photo-Optical Instrumentation Engineers (SPIE) Conference Series*], *Society of Photo-Optical Instrumentation Engineers (SPIE) Conference Series* **7014** (Aug. 2008).

[4] Macintosh, B. A., Graham, J. R., Palmer, D. W., Doyon, R., Dunn, J., Gavel, D. T., Larkin, J., Oppenheimer, B., Saddlemyer, L., Sivaramakrishnan, A., Wallace, J. K., Bauman, B., Erickson, D. A., Marois, C., Poyneer, L. A., and Soummer, R., "The Gemini Planet Imager: from science to design to construction," in [*Society of Photo-Optical Instrumentation Engineers (SPIE) Conference Series*], *Society of Photo-Optical Instrumentation Engineers (SPIE) Conference Series* **7015** (July 2008).

[5] Baudoz, P., Mas, M., Galicher, R., and Rousset, G., "Focal plane wavefront sensor sensitivity for ELT planet finder," in [*Society of Photo-Optical Instrumentation Engineers (SPIE) Conference Series*], *Society of Photo-Optical Instrumentation Engineers (SPIE) Conference Series* **7736** (July 2010).

[6] Galicher, R., Baudoz, P., Rousset, G., Totems, J., and Mas, M., "Self-coherent camera as a focal plane wavefront sensor: simulations," *Astronomy and Astrophysics* **509**, A260000+ (Jan. 2010).

[7] Baudoz, P., Boccaletti, A., Baudrand, J., and Rouan, D., "The self-coherent camera: a new tool for planet detection," in [*IAU Colloq. 200: Direct Imaging of Exoplanets: Science Techniques*], Aime, C. and Vakili, F., eds., 553–558 (2006).

[8] Galicher, R., Baudoz, P., and Rousset, G., "Wavefront error correction and earth-like planet detection by a self-coherent camera in space," *Astronomy and Astrophysics* **488**, L9–L12 (Sept. 2008).

[9] Rouan, D., Riaud, P., Boccaletti, A., Clénet, Y., and Labeyrie, A., "The four-quadrant phase-mask coronagraph. i. principle," *Publications of the Astronomical Society of the Pacific* **112**, 1479–1486 (Nov. 2000).

[10] Abe, L., Domiciano de Souza, Jr., A., Vakili, F., and Gay, J., "Phase Knife Coronagraph. II - Laboratory results," *Astronomy and Astrophysics* **400**, 385–392 (Mar. 2003).

[11] Bordé, P. J. and Traub, W. A., "High-contrast imaging from space: Speckle nulling in a low-aberration regime," *Astrophysical Journal* **638**, 488–498 (Feb. 2006).

[12] Give'On, A., Belikov, R., Shaklan, S., and Kasdin, J., "Closed loop, DM diversity-based, wavefront correction algorithm for high contrast imaging systems," *Optics Express* **15**, 12338–+ (2007).

[13] Poyneer, L. A. and Véran, J.-P., "Optimal modal Fourier-transform wavefront control," *Journal of the Optical Society of America A* **22**, 1515–1526 (Aug. 2005).

[14] Mas, M., Baudoz, P., Rousset, G., Galicher, R., and Baudrand, J., "Self-coherent camera: first results of a high-contrast imaging bench in visible light," in [*Society of Photo-Optical Instrumentation Engineers (SPIE) Conference Series*], *Society of Photo-Optical Instrumentation Engineers (SPIE) Conference Series* **7735** (July 2010).